

Electronic Supporting Information

Microdroplet based Disposable Sensor Patch for Detection of α -amylase in Human Blood Serum

Mitradip Bhattacharjee ^a, Sagnik Middya ^b, Pablo Escobedo^a, Joydip Chaudhuri ^c, Dipankar Bandyopadhyay*^{bc}, and Ravinder Dahiya*^a

^a *Bendable Electronics and Sensing Technologies (BEST) group, University of Glasgow – G12 8QQ, Glasgow, United Kingdom*

^b *Centre for Nanotechnology, Indian Institute of Technology Guwahati - 781039, Assam, India*

^c *Department of Chemical Engineering, Indian Institute of Technology Guwahati - 781039, Assam, India*

*Corresponding author

Emails: dipban@iitg.ac.in; Ravinder.Dahiya@glasgow.ac.uk

I. Fabrication Process of Flexible Substrate

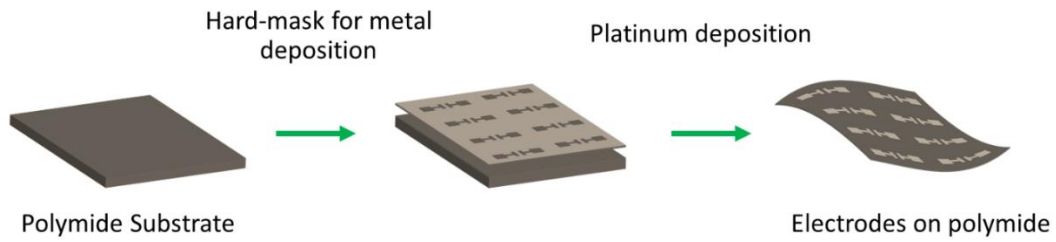


Figure S1: This image shows the fabrication process of the flexible polyamide substrate with Pt electrodes.

The steps for fabrication of the flexible sensor are shown in **Figure S1**. The 50 nm thick Pt on 10 nm Au was deposited to fabricate electrodes with a separation gap of $\sim 40 \mu\text{m}$ on the flexible polyimide substrate using hard-mask. The Au layer was deposited to enhance the adhesion between the substrate and electrodes. The other details of the microdroplet sensor have been shown schematically in the **Figure 1** of the main manuscript. The flexible substrate and the microscopic images of the electrodes are shown in **Figures 4(A) – 4(C)**, respectively.

II. Rotation inside the droplet

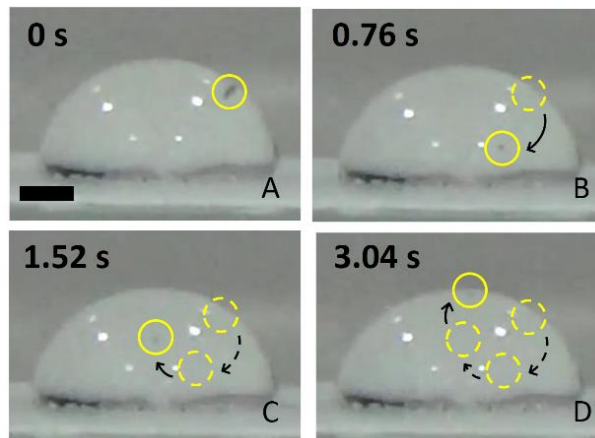


Figure S2: Images (A) – (D) show the side-view of the droplet obtained from the digital camera at different time intervals. In order to illustrate the convective migrations inside the droplet a $\sim 120 \mu\text{m}$ particle was employed and tracked. The circular symbols and the arrowhead on the images show the typical migrations of the microparticle. The scale bar is of 2 mm.

The particle inside the droplet performed a rotational motion under such a situation, as shown in the images (A - D) of **Figure S2**. The rotational motion originated because of the temperature difference across the droplet, which led to, (i) natural convection due to the temperature gradient across the droplet base to drop-surface and (ii) thermal Marangoni motion originating from the gradient in the surface tension across the liquid-air interface of the droplet. The nature of these rotational motions has been investigated in detail with the help of the CFD simulations.

III. Simulation Details

A. Problem Formulation:

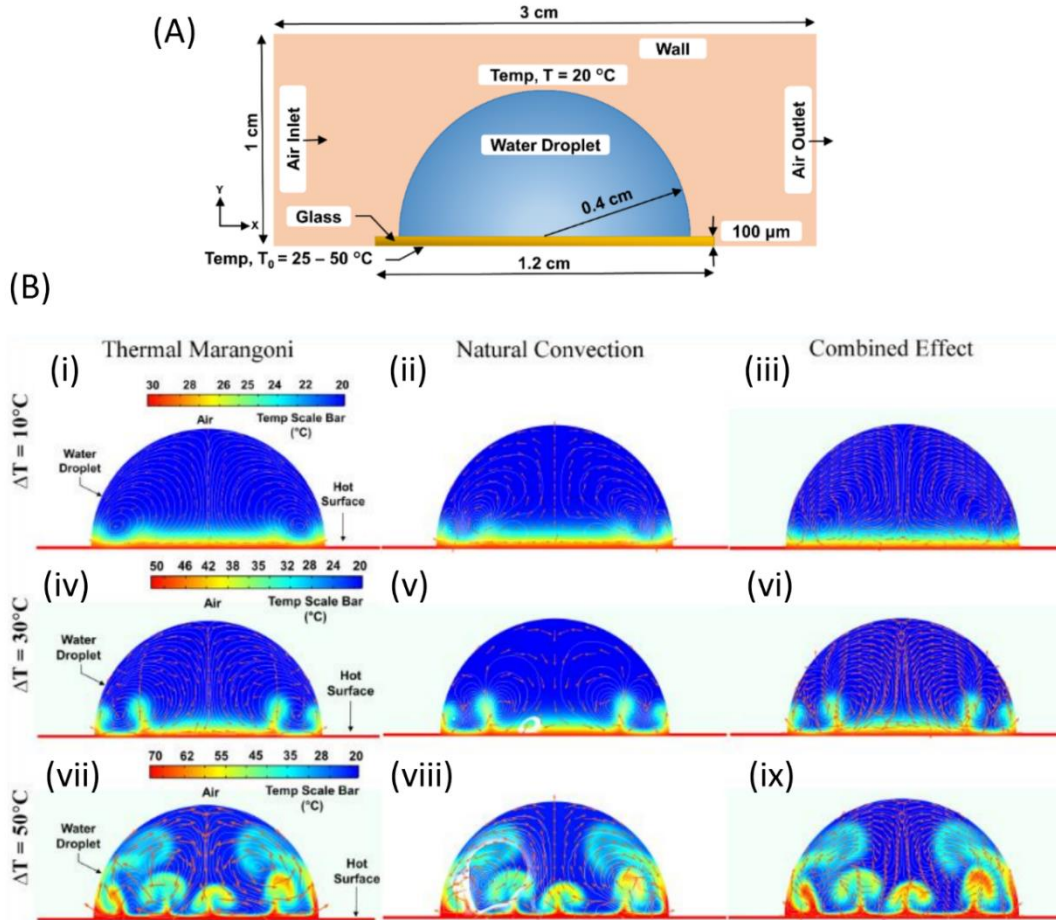


Figure S3: Image (A) shows the schematic diagram of the computational domain employed in this study with the necessary dimensions. The temperature contours in the image set (B) show the rotational motions inside the droplet due to the thermal Marangoni (column (a)), natural convection (column (b)), and combined effect (column (c)). The colored contour, lines, and arrows show the temperature distribution, streamlines, and velocity vectors due to the motion inside the droplet, respectively. Images in the rows (i) - (iii) show the temperature gradient created inside the droplet after, $t = 1$ s, of simulated time when, $\Delta T = 10^\circ\text{C}$, 30°C , and 50°C , respectively.

In this section, a computational analysis was performed to uncover the salient features of the rotational motion due to the combined effects of thermal Marangoni and natural convection inside the droplet. For this purpose, a rectangular domain of length 3 cm and width 1 cm was chosen to be the computational domain, as shown in **Figure S3(A)**. A two-dimensional (2-D) semi-circular water droplet of diameter 8 mm surrounded by air was placed at 0.5 cm downstream of the channel from the inlet. The droplet was placed on a flat and rectangular solid substrate having length 1.2 cm and thickness $100\ \mu\text{m}$, which emulated the experimental system of glass substrate heated from the bottom, as shown in **Figure S3(A)**. In the computational fluid dynamic (CFD) model, air (gas, $i = 1$) and water (liquid, $i = 2$) phases were assumed to be immiscible, and Newtonian. The surface tension of water was modelled as a linear function of the temperature gradient between the hot solid substrate and the fluid domain

(water droplet and surrounding air) as, $\gamma = \gamma_0 + \alpha(\Delta T)$. Here, γ_0 ($= 72.8$ mN/m) was the surface tension of water at 20°C , α was the slope ($= -0.2063$ mN/m $^\circ\text{C}$), (Vargaftik et al. 1983) and ΔT (~ 5 – 30°C) was the temperature gradient between the hot solid surface and the fluid domain.

The density of water was varied with temperature gradient as approximated by Boussinesq (Demuren and Grotjans 2009). According to the approximation, the density of water could be modelled as a linear function of the temperature gradient between the hot solid substrate and the fluid domain (water droplet and surrounding air), $\rho_2 = \rho_0(1 - \beta\Delta T)$. Here, ρ_0 ($= 1000$ kg/m 3) was the density of water at 4°C and β was the thermal expansion coefficient ($= 69 \times 10^{-6}$ K $^{-1}$ at 20°C) (Putintsev and Putintsev 2017). The following continuity and equations of motion were employed to describe the motion of the i^{th} phase,

$$\nabla \cdot \mathbf{u}_i = 0, \quad (1)$$

$$\rho(\dot{\mathbf{u}}_i + \mathbf{u}_i \cdot \nabla \mathbf{u}_i) = \nabla \cdot \left[-p_i \mathbf{I} + \eta_i (\nabla \mathbf{u}_i + \nabla \mathbf{u}_i^T) \right] + \mathbf{f}_{st} + \rho \mathbf{g}. \quad (2)$$

The velocity vector, density, viscosity, and pressure of the i^{th} phase were denoted by notations \mathbf{u}_i , ρ_i , η_i , and p_i respectively. The over-dot symbol denotes the time derivative and \mathbf{g} signified the acceleration due to gravity vector, which was assumed to operate in the negative y-direction.

The surface tension force was defined as, $\mathbf{f}_{st} = G \nabla \phi$, a product of the chemical potential (G) and the gradient of the phase field parameter (ϕ). The surface tension force was determined by minimizing the total free energy inside fluid domain as a function of the phase field variable (ϕ),

$$F(\phi) = \int_{\Omega} \left(f(\phi) + \frac{1}{2} \lambda |\nabla^2 \phi| \right) d\Omega. \quad (3)$$

Where, Ω was computational volume and the total free energy, $F(\phi)$ was a combination of double well potential, $f(\phi) = \lambda/4N^2(\phi^2 - 1)^2$, and surface energy. The parameter N was calculated by the following equation, $N = 0.5h_m$ where h_m was the maximum element size in the computational domain. To evaluate surface energy, mixing energy density (λ) was estimated as, $\lambda = (3\gamma N)/(2\sqrt{2})$ in which γ was surface tension and N was the thickness of the diffused interface.

In order to track the rotational Marangoni motion of the droplet at the air-water interface and in the bulk, the phase-field method was employed (Jacqmin 1999; Lin et al. 2012; Sharma et al. 2015; Sharma et al. 2014; Timung et al. 2017). In this method, the transport equation was written in terms of the phase field parameter (ϕ) as,

$$\dot{\phi} + \mathbf{u}_i \cdot \nabla \phi = \nabla \cdot \chi(\nabla G). \quad (4)$$

Where, the chemical potential (G) is defined as a derivative of the free energy functional, $G = F'(\phi) = \lambda \left[-\nabla^2 \phi + \phi(\phi^2 - 1)/N^2 \right]$. The interfacial density (ρ), and viscosity (μ) were evaluated in terms of f as, $a = 0.5[a_1(1 + \phi) + a_2(1 - \phi)]$, where a can be any of ρ and μ . The

symbol χ represents the mobility tuning parameter, which was chosen to be 10 m s/kg to avoid mass loss in the conventional phase field model.

In order to identify the temperature distribution across the droplet, and subsequently calculate the temperature dependent surface tension at the liquid-air interface, the generalized advection-diffusion equation for heat-transfer was employed for the liquid droplet,

$$\rho C_p \frac{\partial T}{\partial t} + \rho C_p \mathbf{u}_i \cdot \nabla T - k \nabla^2 T = 0. \quad (5)$$

In order to model the heat-transfer through the solid substrate, the following heat diffusion equation was considered,

$$\rho C_p \frac{\partial T}{\partial t} - k \nabla^2 T = 0. \quad (6)$$

In the Eqs. (5) and (6), C_p was the heat capacity of the solid or liquid material, k was the thermal conductivity of the solid or liquid material, and T was the temperature.

Boundary Conditions:

Among the hydrodynamic boundary conditions, the lower flat surface of the droplet was assumed to be non-slipping and impermeable for both the fluids while the curved air-water interface was considered to be the deformable one. The velocity of air and liquid at the inlet and outlet were set to zero. The upper wall of the computational domain was assumed to be non-slipping and impermeable for both the fluids. The contact angle of water droplet on the bottom substrate was considered to be 90° unless mentioned otherwise (Bhattacharjee et al. 2016). As we have discussed previously, in this computational work, the droplet was placed on a rectangular solid substrate having length of 1.2 cm and thickness 100 μm , emulating the glass surface resting on a heater. In order to model the heat-transfer characteristics of this system accurately, we assumed that the lower surface of the 1.2 cm \times 100 μm rectangular domain to be at constant temperature T_0 and the variable T_0 was set to the experimentally measured temperature of the hot plate, as shown in the **Figure S3(A)**. The temperature of this lower surface was varied in the different simulations to achieve the different thermal gradients across the droplets. In contrast, at the upper surface and at the side surfaces of the 1.2 cm \times 100 μm rectangular domain at the base of the droplet we equated the heat flux due to conduction of the solid to the heat flux due to convection of the fluids. Apart from this rectangular domain at the basement of the droplet, we modeled the remaining lower surface and the upper surface of the outer rectangular domain (size 3 cm \times 1 cm) to be thermally insulated. Finally, at the inlet and outlet we enforced constant temperature boundary conditions for both the fluids.

Solution Methodology:

The unsteady governing equations (1) – (6), and the boundary conditions were solved using the commercially available COMSOLTM Multiphysics software based on the finite element method. In this method, the spatial terms of the governing equations were initially discretized to obtain an ordinary differential equation (ODE) in time, which was time-marched to obtain the evolution of the streamline flow patterns inside the droplet. The 2-D geometry was divided into ~87653 triangular elements to obtain the grid independent solutions. We employed the built-in Galerkin least-square (GLS) method to discretize nonlinear convective diffusion

equations, which was stabilized through streamlining and crosswind diffusions. The segregated predictor-corrector method had been used to obtain the velocity and pressure profiles by incremental pressure correction.

Rows (i) – (iii) in the **Figure S3(B)** show the temperature gradient contours inside the droplet after $t = 1$ s of simulation for $\Delta T = 10^\circ\text{C}$, 30°C , and 50°C , respectively. It is quite evident from the contour plot that, there is a sharp thermal gradient (for example, 3×10^6 $^\circ\text{C}/\text{m}$ for $\Delta T = 30^\circ\text{C}$ case) created near the contact line of the water droplet. Consequently, the surface tension and density of water reduce significantly near the contact line of the droplet because both of these parameters are modeled as linearly decreasing functions with the temperature gradient. In such a scenario, ambient temperature (20°C) at the free surface of the droplet establishes a surface tension (thermal) gradient suitable for Marangoni (natural) convection. Subsequently, the rotational motions inside the droplet is observed, which is shown by the streamlines and the velocity vectors on the images in the **Figure 3(B)**.

The columns (a) and (b) show the rotational motions computed from the simulations inside the droplet, which was solely due to the thermal Marangoni and natural convections. The combined influence of these two convective rotations is summarized in the column (c). It can be visualized from the images that, for a particular temperature gradient, the rotational flow due to surface tension gradient occurs throughout the droplet whereas, the rotational flow due to natural convection occurs only in the vicinity of the local hot spots inside the droplet-like near the contact line of the droplet. For lower temperature gradients like, $\Delta T = 10^\circ\text{C}$, the thermal Marangoni flow is comparatively higher than the rotations due to natural convection as illustrated in images (i – iii), whereas, for higher temperature gradients like, $\Delta T = 50^\circ\text{C}$, flow due to natural convection overpowers the effect of thermal Marangoni flow as shown in images (vii – ix). In the moderate temperature gradients like, $\Delta T = 30^\circ\text{C}$, both the effects of natural convection and thermal Marangoni are present inside the water droplet as illustrated in images (iv – vi). In summary, both the thermal Marangoni flow and natural convection creates the rotational motion inside the droplet for all the temperature gradients, however the dominance of thermal Marangoni (natural convective) flow is higher in the lower (higher) temperature gradients.

The simulated results shown above help in optimizing the sensor fabrication protocol. Intuitively, a very hot metal substrate should always be avoided because that may lead to rapid evaporation of the water droplet. Further, an insulator substrate is always suitable for the electrode fabrication of the electrochemical sensor. It is well known that enzymes can be heat sensitive, which require optimization of the thermal gradient (ΔT) where $\Delta T = T - T_0$, where $T_0 \sim 22^\circ\text{C}$ and T is the temperature of the substrate. In addition, at a larger ΔT , the recirculation due to natural convection inside a droplet can become turbulent, which can destabilize the electrical signals extracted from the sensor. In this regard, a steady and patterned rotational motion inside the droplet is always preferable. The simulations shown above corroborate that a smaller rotational current during NC in conjunction with the TM motion can provide an optimal mixing and hence an electrical response for the sensor. Thus, in order to optimize these aspects, in what following we explore the influence of the thermal conductivity of the underlying substrate, droplet size, applied thermal gradient, viscosity and thermal conductivity

of the droplet, and the surface properties of the substrate and the droplet on the rotational currents inside the droplet.

Figure 3(A) shows the effect of thermal conductivity (k) of the solid surface on the average rotational speed (ω_{Avg} , Avg, circular symbol) inside the droplet when its thermal conductivity (k) is kept unchanged. In such a scenario, an enhancement in the rate of heat transfer of the hot substrate establishes a larger temperature gradient between the substrate-droplet interface. We observe a higher ω_{Avg} under this condition owing to the increase in the Thermal Marangoni motion (ω_{TM} , square symbol) as well as natural convection (ω_{NC} , triangular symbol). It may be noted here that the k values in the simulations have been selected based on the same observed for the different materials such as glass (0.8 W/mK), mercury (7.82 W/mK), lead (35.6 W/mK), tin (68.2 W/mK), iron (86.5 W/mK), and copper (385 W/mK). (Vargaftik et al. 1983)

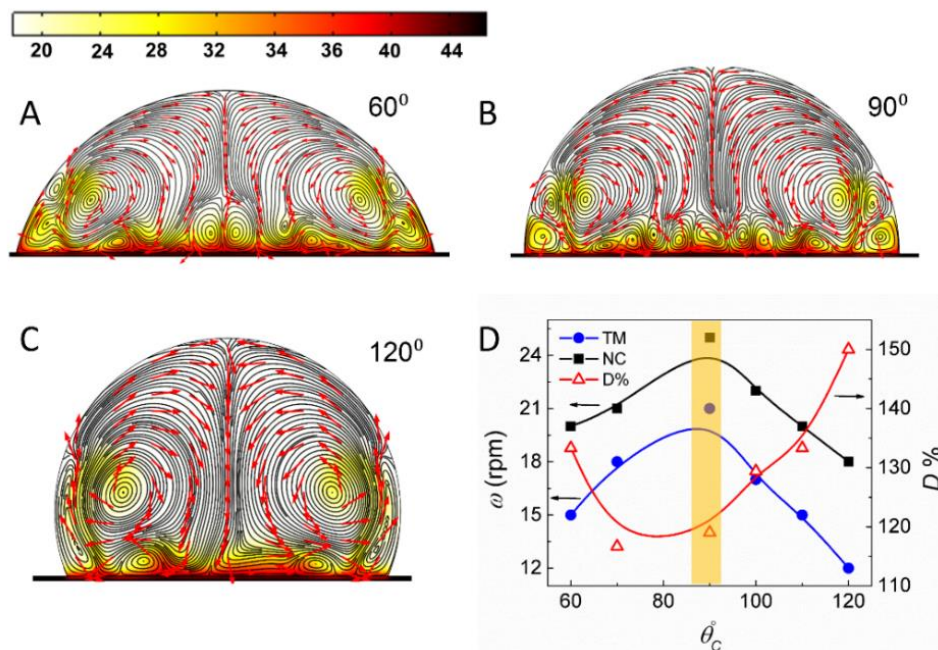


Figure S4: Images (A) to (C) show the effect of contact angle (θ_c) on the motion inside the droplet. Image (D) shows the change in rotation (ω) due to different contact angle values. Dependence of dominance (D) with contact angle is also illustrated in the image (D). The temperature of the substrate in this case was maintained at 50°C.

Interestingly, all the ω versus k plots in the **Figure 3(A)** suggest that, beyond a critical value of $k = k_c$ (~ 100 W/mK), the rotational motion increases sharply, as indicated by the drastic change in the slope of the plots. The plots also suggest that $\omega_{NC} \gg \omega_{TM}$ beyond k_c , which is demarcated by light and dark gray zones. The plot associated with the ratio of rotational strength, $R_\omega = (\omega_{NC}/\omega_{TM})$ or dominance $D = (NC/TM) \times 100\%$, uncover the enhancement in the relative strength of the rotational motions due to NC and TM. This plot suggests $\omega_{NC} \sim \omega_{TM}$ until about k_c while $\omega_{NC} \gg \omega_{TM}$ when $k \gg k_c$. **Figure 3(A)** show that a Cu surface with higher $k \sim 385$ W/m K is expected to facilitate a stronger and more random NC inside the droplet owing to coherent nature of the convective vortices. In contrast, on a glass substrate

with lower $k \sim 0.8$ W/m K the rotational motions originating from the TM and NC are equally strong leading to laminar and structured vortices inside the droplet. Thus, the latter, case is found to be more suitable for the proposed sensor, which is discussed in the later part of the manuscript.

Figure 3(B) shows the effect ΔT on ω_{Avg} , which suggests that as the temperature gradient across the hot substrate and droplet increases (from 0.5×10^6 °C/m to 3×10^6 °C/m) higher rotational motions due to NC and TM are observed. The increase ω_{TM} and ω_{NC} can be attributed to the higher surface tension and thermal gradients. Again, all the ω versus k plots in the **Figure 3(B)** suggests that, beyond a critical ΔT_c (~ 20), the rotational motion increases sharply, as indicated by the drastic change in the slope of the plots. The plots also suggest that $\omega_{NC} \gg \omega_{TM}$ beyond ΔT_c , which is again demarcated by light and dark gray zones. The plot associated with, D , uncover $\omega_{NC} \sim \omega_{TM}$ until ΔT_c while $\omega_{NC} \gg \omega_{TM}$ when $\Delta T > \Delta T_c$. The results shown in the **Figure 3(B)** suggest an operating temperature of $\sim 40 - 45^\circ\text{C}$ of the underlying substrate for the laminar and structured vortices originating from the almost equally strong TM and NC, suitable for the proposed sensor. Importantly, the variations in ω_{Avg} with ΔT followed the computational predictions until the operating zone identified ($\Delta T = 20 - 25^\circ\text{C}$), as shown by the square symbols on the **Figure 3(B)**.

In fact, the operating temperature and thermal gradient are also found to be optimal from the perspective of droplet evaporation because under this condition we extracted enough rotational motion necessary for the stable electrical response of the droplet with minimal evaporation of the same. Further, the operating temperature is also found to be suitable for optimal enzyme activity and its chemical stability. Images (A) to (C) in the **Figure S4** shows the variations in the streamlines, velocity vector, and temperature across a droplet when the contact angle (θ_C) between the droplet and the substrate is varied. Image (D) shown the variations in ω_{TM} , ω_{NC} , and ω_{Avg} with the variation in θ_C when $\Delta T = 20$ °C and $k = 0.8$ W/m K. Images (A) to (C) suggest that a droplet having higher contact angle has symmetric vortices inside the droplet. However, a very high contact angle reduces the area of contact between the droplet and the substrate, which poses problem in extracting the electrical signal from the base of the droplet. Moreover, image (D) shows that the droplet shows a highest rotational motion for a contact angle of, $\theta_C \sim 90^\circ$. Further, the $\theta_C \sim 60^\circ$ also gives an advantage in terms of high dominance factor with sufficiently high rotational motion. Thus, contact angle close to those values would be highly preferable for this application. Importantly, under such a condition, the rotational motions originating from the TM and NC are equally strong leading to a laminar flow inside the droplet, as reflected in D versus ω_{Avg} plot in the image (D). The experiments suggest that the use of a commercially available hydrophobic polymer on the glass substrate as a film can ensure the droplet configuration with, $\theta_C \sim 86^\circ$, as shown in the image (B). Importantly, the thermal properties of the polymer are very similar to the glass, which enable an identical thermal response suitable for the sensor. Concisely, the simulations shown in **Figure S4** help in optimizing the shape and surface properties of the droplet and the substrate.

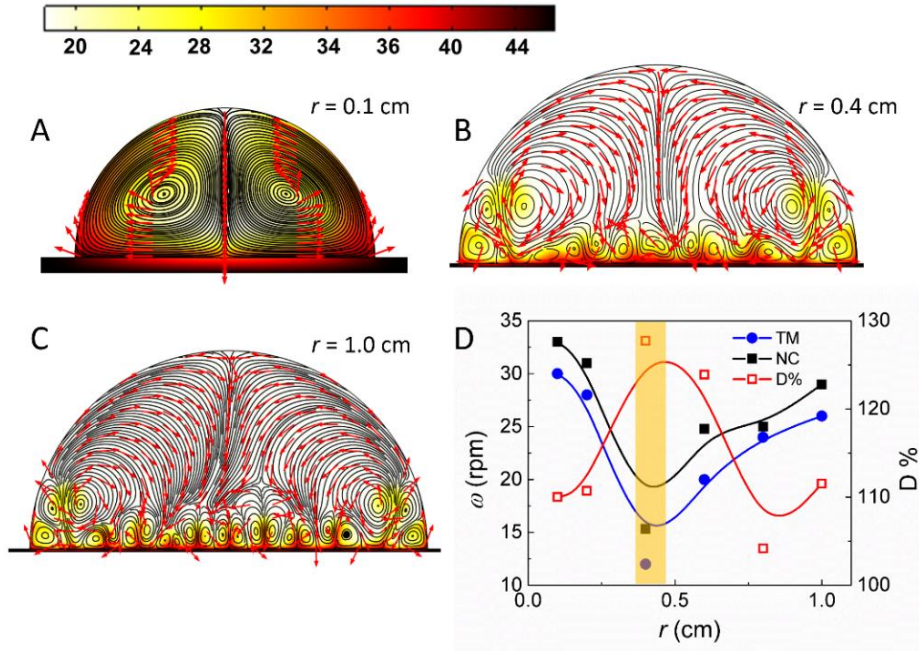


Figure S5: Images (A) to (C) show the effect of droplet volume on the motion inside the droplet. Image (D) shows the change in rotation (ω) due to change in the radius (r) of the droplet. Dependence of dominance (D) with droplet radius (r) is also illustrated in the image (D). The temperature of the substrate in this case was maintained at 50°C .

Figure S5 shows the effect of size of the droplet on its hydrodynamic characteristics. Images (A) to (C) of **Figure S5** show the variations in the streamlines, velocity vector, and temperature across the droplet due to change in its radius (r). Image (D) **Figure S5** shown the variations in ω_{TM} , ω_{NC} , and ω_{Avg} with r when $\Delta T = 20$ and $k = 0.8$ W/m K. The simulations suggest that the droplets with smaller volume show a higher ω_{Avg} with more symmetric rotational patterns when compared with the bigger droplets. However, a very small droplet also suffers from the possibility of faster evaporation under the existing thermal gradient. On the other hand, a very big droplet shows a large number of smaller vortices near the substrate, a signature of extensive Rayleigh-Bennard instability due to NC. Thus, we avoid the zone of hydrodynamic instability for the bigger droplets, which cause fluctuations in electrical response. Keeping all these aspects in mind, an operating droplet radius of $r = 0.1 - 0.4$ cm has been identified where $R_\omega = 1.1 - 1.2$ or $D = 110 - 120\%$, as shown in the image (D). The experiments suggest that the electrical and thermal stabilities of such microdroplets are optimum for the sensing application.

IV. Contact Angle Measurement on Bended Surfaces

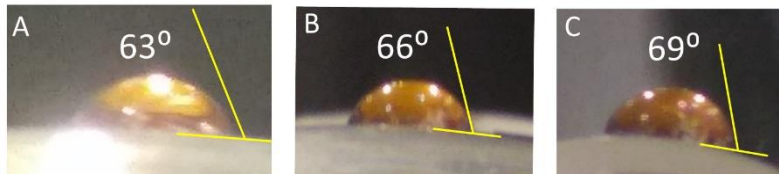


Figure S6: Images (A) to (C) show the contact angle of a microdroplet with diameter ~ 3.5 mm on three bended polyimide surfaces having bending radius (r_b) of 2.8 cm, 1.8 cm, and 1.1 cm respectively.

Experiments were performed to measure the effective contact angle of the droplet at different bending conditions. The contact angle was measured from the optical images of the droplets on polyimide substrates at different bending conditions. Polyimide substrates were initially attached on bended rigid substrates having different bending radius using double sided tapes and then images were captured from the side using digital camera. Thereafter, the angles were measured by post processing the captured images. Images (A) to (C) of **Figure S6** show the contact angle of a microdroplet with diameter ~ 3.5 mm on three bended polyimide surfaces having bending radius (r_b) of 2.8 cm, 1.8 cm, and 1.1 cm, respectively.

V. Temporal Response of Sensor, Reaction Mechanism, and Control Experiments

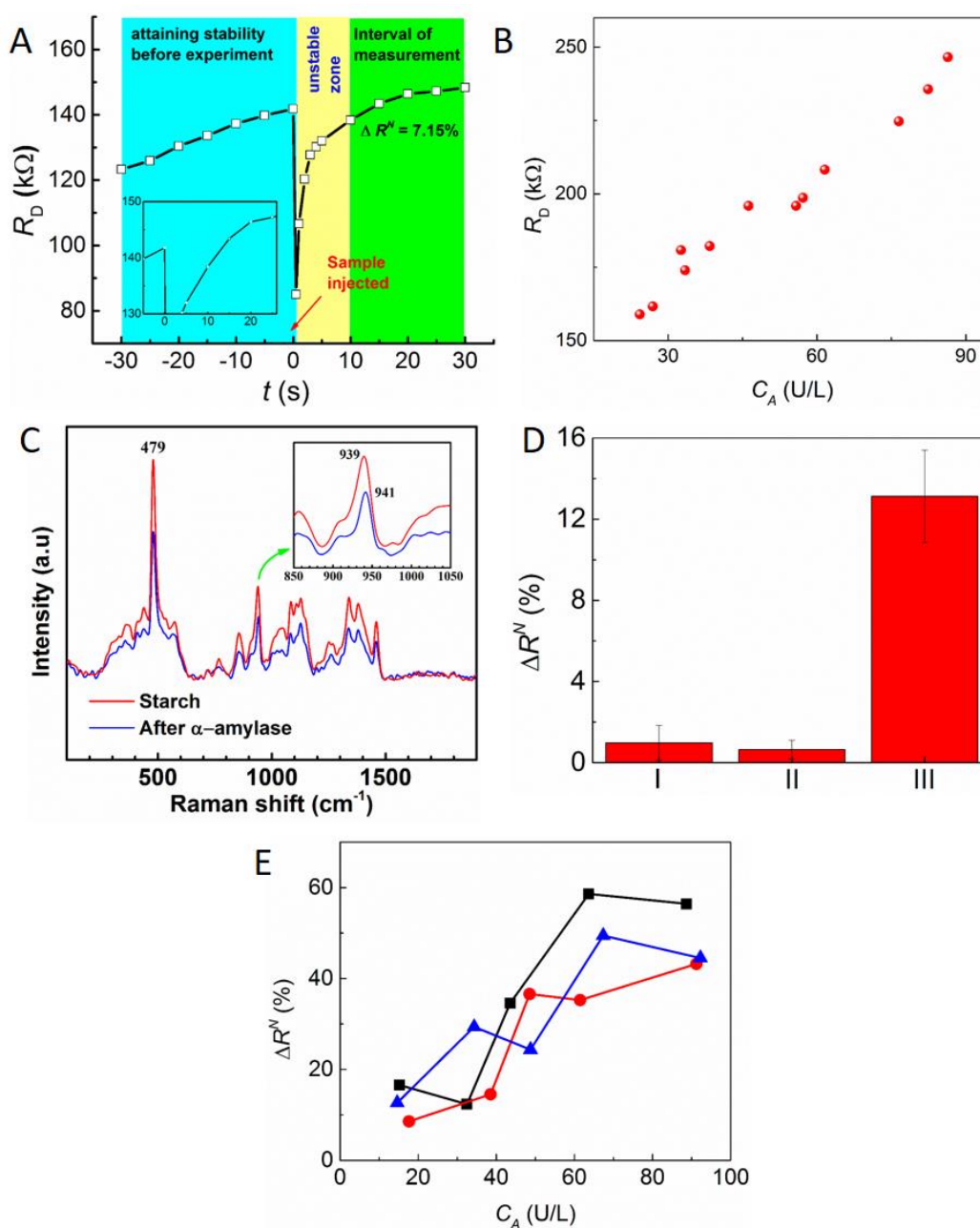


Figure S7: (A) shows the temporal response of the sensor for $C_A = 20$ U/L of amylase at a substrate temperature of 26 $^{\circ}$ C and the image in the inset shows the zoomed portion of the plot, (B) Resistance response (R_D) of the sensor for different amylase concentration, (C) Raman

spectroscopy of starch-amylase reaction, (D) control experiment results with and without starch and amylase, (E) control experiment of the sensor without heat.

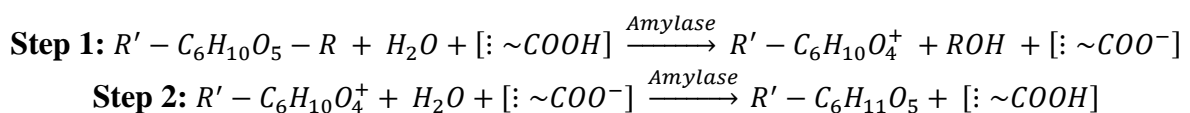
(VA) Temporal Response:

Figure S7(A) shows the temporal response of the sensor for $C_A = 20$ U/L of amylase at a substrate temperature of 26°C. The sensor showed ~7.15% change in the normalized resistance. The plot in inset shows the magnified view where the difference between the initial and final resistances is clearly visible. The change in response occurred due to the reaction between the starch and amylase, as described in the reaction mechanism section (VB). Further, the resistance response for different concentration of amylase is given in **Figure S7(B)**. The plot shows the resistance across the droplet at different concentrations of amylase. The resistance was recorded after 30 s of the addition of amylase in to the sensing droplet.

(VB) Reaction Mechanism:

Starch polymers were largely α -1,4 – glucans with α -1,6 branches in a very small percentage. The average size of the starch granules was in micron range whereas the hydrodynamic radius of the enzyme was 3-4 nm. Thus, the glycosidic linkages mostly acted as a potential site of attack for the α -amylase. In a way, the enzyme, an endo-acting α -1,4–glucan hydrolase, catalyzed hydrolysis of solid granular starch wherein the enzyme diffused through the surface of the starch molecules to initiate the degradation (Colonna et al. 1992). The granules provided more sites for adsorption of the enzymes (Payan et al. 1980). The starch had localized subsites that were potential binding area as the subsites could be filled with glucan residues. Human pancreatic α -amylase contained five binding sites that target the active sites and cleavage occurred when maltose acted as a leaving group. The α -amylase selectively hydrolyzed starch into maltose (Butterworth et al. 2011; Mishra et al. 2002; Moore et al. 2015). Further, the mixing vortices generated inside the droplet through thermal excitation facilitated such a reaction.

According to the prior art (Chiba 1997; Kaneko et al. 1999; Kempton and Withers 1992), the starch-amylase reaction often leads to an excess of intermediate protonated carboxyl and oxocarbenium ions, which is related to the increase in resistance across the droplet, R_D , as explained below. The starch amylase reaction can be represented as the following simplified two-step process,



Where $R' - C_6H_{10}O_5 - R$ is the starch, R' and R represent the glucose units before and after the glycosidic linkage, and $[:\sim COOH]$ represents the carboxylic group in the amino acid residues of amylase that executes the hydrolysis.

In step 1, the glycosidic bond between the α -C and —OR is cleaved, and the —OR⁻ extracts H⁺ from —COOH group of the amylase enzyme. Thus, the hydrolysis product ROH is formed, leaving behind —COO⁻ group, as illustrated in the step 1. By the bond cleavage at the α -C, a positively charged oxocarbenium ($R' - C_6H_{10}O_4^+$) ion is produced. Eventually, the —COO⁻

group on the amylase assists in the addition of another H₂O molecule to the oxocarbenium ion, as illustrated in step 2. Subsequently, the catalytic ionizable group of amylase creates excess protonated carboxyl ions, as illustrated above (Chiba 1997; Kaneko et al. 1999; Kempton and Withers 1992). Due to the presence of comparatively bulkier excess protonated carboxyl ions, the conductance across the droplet reduces, as the effective ion movement reduces. Hence, the R_D increases. Besides, in the process of hydrolysis, an oxocarbenium ion (positive charged) is produced on the starch molecule, as described in step 1 of the reaction. This ion also indirectly adds to the excess protonated carboxyl ions in the system. Apart from these, Fe²⁺ ions from the electrolyte interact with negatively charged amino acid residues (e.g. aspartic acid, glutamic acid) of amylase. Because of this interaction between opposite charges, the transporting ions reduce. Naturally, a higher increase in R_D has been expected for a higher concentration of amylase, as more amylase leads to more interaction.

In order to characterize the concept, we performed a Raman spectroscopy, as illustrated in **Figure S7(C)**. The 476 – 480 cm⁻¹ band represented the vibration of the whole molecule of starch while it was absent in glucose or maltose (Santha et al. 1990). In our case, the position of the peak at 479 cm⁻¹ remained unaltered after amylase treatment. However, the intensity decreased owing to the change in skeletal vibration. The 936 – 940 cm⁻¹ band in the fingerprint region, was the vibration signature of the characteristic α -1,4 glycosidic linkages of starch (Kim et al. 1989; Santha et al. 1990). As depicted in the inset, the 939 cm⁻¹ peak shifted to 941 cm⁻¹ after α -amylase treatment. This indicated the deformation of the bonds caused by starch-amylase interaction. The reduced peak magnitude also confirmed the bond cleavage.

(VC) Control Experiments:

Figures S7(D) and **S7(E)** show two control experiments. In **Figure S7(C)**, three experiments were performed with a droplet sensor (I) without amylase, (II) without starch, and (III) droplet with starch and ~17.3 U/L amylase. The sensor showed almost no response without amylase, and starch. However, the addition of very low concentration (~17.3 U/L) of amylase showed a significant response. Similarly, experiments were also performed without heat. It was observed that without heat the response of the sensor was rather random, as illustrated in **Figure S7(E)**.

VI. Stability of the Sensor

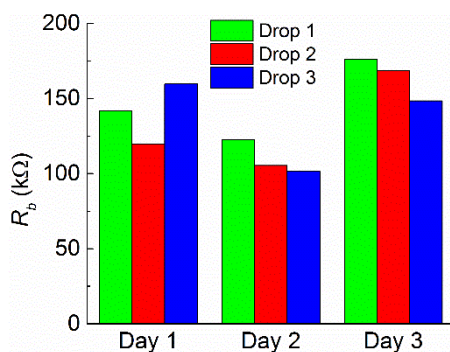


Figure S8: This figure shows the base resistance (R_b) of three different droplets for three different days.

The stability of the sensor was also checked by measuring the base resistance of droplets from 3 different freshly prepared solutions for 3 different days, as illustrated in **Figure S8**. The plot suggests that the droplet solution was stable and reusable for the experiments. The base resistance of the individual droplet preparations showed a decrease between day 1 and day 2, and an increase on day 3. It is important to note that in this case, the results show the value of base resistance of the droplet. As long as the droplets showed a base resistance value in the same order, the system associated with the sensing could be calibrated. In this case, the change was 1.1-1.5 times, which indicated that the sensor performance was considerably good for at least for 3 days. However, one has to consider the effect of manual placement of the drop on the electrodes, and storage of the fluid, which might also had been a source of variations. Possibly, this was the reason behind the variation among individual droplets on a day.

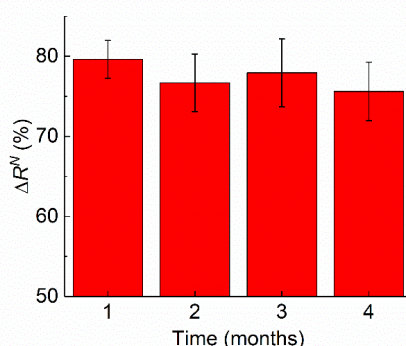


Figure S9: This figure shows the stability of the flexible sensing patch with time. The concentration amylase was ~ 90 U/L for the measurements.

The stability of the flexible sensing patches was also studied as shown in **Figure S9**. A single batch of sensors was tested for 4 months and the response was found stable. Hence, the sensing patch could be stored for more than 4 months, which made it viable for long-term use. The concentration of amylase in the stability study of Figure S9 was ~ 90 U/L.

VII. Brief Description of Supporting Video

Supporting Video S1: A droplet was kept on a hot substrate at $\Delta T \sim 20^\circ\text{C}$. the graphite particles inside the droplet shows the rotational motion due to the combined effect of thermal Marangoni and natural convection.

References:

- Bhattacharjee, M., Pasumarthi, V., Chaudhuri, J., Singh, A.K., Nemade, H., Bandyopadhyay, D., 2016. *Nanoscale* 8(11), 6118-6128.
- Butterworth, P.J., Warren, F.J., Ellis, P.R., 2011. *Starch - Stärke* 63(7), 395-405.
- Chiba, S., 1997. *Bioscience, Biotechnology, and Biochemistry* 61(8), 1233-1239.
- Colonna, P., Leloup, V., Buléon, A., 1992. *European Journal of Clinical Nutrition* 46(2), S17-32.
- Demuren, A., Grotjans, H., 2009. *Numerical Heat Transfer, Part B: Fundamentals* 56(1), 1-22.
- Jacqmin, D., 1999. *Journal of Computational Physics* 155(1), 96-127.

Kaneko, H., Kuriki, T., Okada, S., 1999. *Journal of Applied Glycoscience* 46(2), 187-197.

Kempton, J.B., Withers, S.G., 1992. *Biochemistry* 31(41), 9961-9969.

Kim, I.-H., Yeh, A.-I., Zhao, B.L., Wang, S.S., 1989. *Biotechnology Progress* 5(4), 172-174.

Lin, Y., Skjetne, P., Carlson, A., 2012. *International Journal of Multiphase Flow* 45, 1-11.

Mishra, P.J., Raguath, C., Ramasubbu, N., 2002. *Biochemical and Biophysical Research Communications* 292(2), 468-473.

Moore, S.A., Ai, Y., Chang, F., Jane, J.-l., 2015. *Carbohydrate Polymers* 115, 465-471.

Payan, F., Haser, R., Pierrot, M., Frey, M., Astier, J.P., Abadie, B., Duée, B., Buisson, G., 1980. *Acta Crystallographica Section B* 36(2), 416-421.

Putintsev, N.M., Putintsev, D.N., 2017. *Journal of Thermal Science* 26(2), 125-131.

Santha, N., Sudha, K.G., Vijayakumari, K.P., Nayar, V.U., Moorthy, S.N., 1990. *Proceedings of the Indian Academy of Science* 102, 705-712.

Sharma, A., Chaudhuri, J., Kumar, V., Timung, S., Mandal, T.K., Bandyopadhyay, D., 2015. *RSC Advances* 5(37), 29545-29551.

Sharma, A., Tiwari, V., Kumar, V., Mandal, T.K., Bandyopadhyay, D., 2014. *ELECTROPHORESIS* 35(20), 2930-2937.

Timung, S., Chaudhuri, J., Borthakur, M.P., Mandal, T.K., Biswas, G., Bandyopadhyay, D., 2017. *ELECTROPHORESIS* 38(11), 1450-1457.

Vargaftik, N.B., Volkov, B.N., Voljak, L.D., 1983. *Journal of Physical and Chemical Reference Data* 12(3), 817-820.